Scripta Materialia 148 (2018) 33–36

Contents lists available at ScienceDirect

Scripta Materialia

journal homepage: www.elsevier.com/locate/scriptamat

Regular article

Radiation resistance of oxide dispersion strengthened alloys: Perspectives from in situ observations and rate theory calculations

Xiang Liu [a,*], Yinbin Miao [b], Meimei Li [b], Marquis A. Kirk [b], Guangming Zhang [c], Shigeharu Ukai [d], Stuart A. Maloy [e], James F. Stubbins [a,f]

[a] Department of Nuclear, Plasma, and Radiological Engineering, University of Illinois at Urbana-Champaign, Urbana, IL 61801, USA
[b] Nuclear Engineering Division, Argonne National Laboratory, Lemont, IL 60439, USA
[c] Qingdao University of Technology, Qingdao, Shandong 266033, China
[d] Materials Science and Engineering, Faculty of Engineering, Hokkaido University, N13, W-8, Kita-ku, Sapporo, Hokkaido 060-8628, Japan
[e] Materials Science and Technology Division, Los Alamos National Laboratory, Los Alamos, NM 87545, USA
[f] International Institute for Carbon Neutral Energy Research (WPI-I2CNER), Kyushu University, 744 Motooka, Nishi-ku, Fukuoka 819-0395, Japan

ARTICLE INFO

Article history:
Received 21 November 2017
Received in revised form 9 January 2018
Accepted 15 January 2018
Available online 9 February 2018

Keywords:
Oxide dispersion strengthened (ODS) alloy
Dislocation structure
Microstructure
Transmission electron microscopy
Radiation enhanced diffusion (RED)

ABSTRACT

Here, in situ ion irradiation and rate theory calculations were employed to directly compare the radiation resistance of an oxide dispersion strengthened alloy with that of a conventional ferritic/martensitic alloy. Compared to the rapid buildup of dislocation loops, loop growth, and formation of network dislocations in the conventional ferritic/martensitic alloy, the superior radiation resistance of the oxide dispersion strengthened alloy is manifested by its stable dislocation structure under the same irradiation conditions. The results are consistent with rate theory calculations, which show that high-density nanoparticles can significantly reduce freely migrating defects and suppress the buildup of clustered defects.

Advanced nuclear reactor systems with inherent safety features are being developed as reliable and sustainable clean energy sources. However, the harsh reactor environment, especially high-dose neutron irradiation (>100 dpa), rules out the extended use of most conventional structural materials. By introducing ultra-stable, high-density (~10^{23} n/m^3) dispersoids to suppress radiation-induced defect formation, nanostructured oxide dispersion strengthened (ODS) alloys represents one of the most promising candidate materials for structural applications in advanced reactors [1]. Commonly used dispersoids are Y-Ti-O nanoparticles (2–4 nm) in ODS Fe-Cr alloys and relatively coarse (~10 nm) Y-Al-O nanoparticles in ODS FeCrAl alloys [2–4]. The stability of these nanoparticles under irradiation or high temperature heat treatment has been demonstrated by several studies [5–12].

A previous review paper [1] compared the helium bubbles in ODS alloy MA957 versus the bubbles in reduced-activation martensitic alloys Eurofer97 and F82H, and found that the helium bubbles in irradiated ODS alloys tend to have higher number density and smaller size, which was also confirmed by a recent study [13]. It is suggested that the nanoparticles in ODS alloys help absorb helium atoms and protect the grain boundaries from helium embrittlement. These findings provide some ideas about the enhanced radiation resistance of ODS alloys. However, most existing studies rely on the ex situ irradiation data and often the comparisons could only be made on alloys with distinct chemical composition, heat treatment, initial microstructure, and irradiation history. Moreover, to the best of our knowledge, few data on the evolution of the dislocation structure, which is closed related to irradiation hardening, of ODS alloys versus non-ODS alloys under similar irradiation conditions could be found in literature.

To identify the differences in the radiation response, especially the evolution of the dislocation structure, bewteen ODS alloys and non-ODS alloys, this study employed in situ transmission electron microscopy (TEM) with concurrent ion irradiation so that a direct comparison of the microstructure changes in different alloy systems under the same exposure conditions is possible. The in situ capability also allows the dynamic observation of the microstructure evolution of exactly the same area over a range of dose levels. In this study, the comparison was made between a Fe-9Cr ODS ferritic/martensitic (F/M) alloy (designated 9CrODS) and a Fe-9Cr F/M alloy, T91. The 9Cr alloys belong to the high Cr alloy family that shows promising resistance to void swelling and irradiation creep [14]. Table 1 shows the nominal chemical composition of the as-received materials.

The as-received T91 and 9CrODS underwent similar heat treatment: T91 was normalized at 1037 °C for 1 h, air cooled, and then tempered at

* Corresponding author.
E-mail address: xliu128@illinois.edu (X. Liu).

https://doi.org/10.1016/j.scriptamat.2018.01.018
1359-6462/

Table 1
Nominal chemical composition of as-received T91 and 9CrODS alloys, in wt.%.

Alloy	Fe	Cr	C	Si	Mn	Ni	W	N	Mo	Nb	Ti	Y	O	Y_2O_3
T91	Bal.	9.24	0.089	0.28	0.47	0.16	–	0.035	0.96	0.054	0.002	–	0.008	–
9CrODS	Bal.	9.08	0.14	0.06	0.09	0.03	1.97	0.013	–	–	0.23	0.29	0.16	0.37

760 °C for 1 h and air cooled, and 9CrODS was normalized at 1050 °C for 1 h, air cooled, followed by tempering at 800 °C for 1 h and air cooled.

The in situ ion irradiation experiments were performed at the IVEM-Tandem facility, Argonne National Laboratory (ANL). The experimental setup was identical to the one previously described by Liu et al. [15]. A Hitachi 9000 NAR electron microscope operated at 200 kV was used for post-irradiation TEM imaging. The incident ion beam was 30° to the electron beam and on average ~15° to the foil normal. TEM thin foils were irradiated by 1 MeV Kr^{++} ions at 400 °C up to 4.2×10^{15} ions/cm^2, corresponding to 7.0 dpa under the Kinchin-Pease option using SRIM calculation with displacement energy set to 40 eV [16,17]. The ion flux was kept at 6.25×10^{11} ions/(cm^2·s), representing a dose rate of 1.0×10^{-3} dpa/s in the thin foil region and the Kr^{++} ions were sufficiently energetic to pass through the foil.

In order to make the comparison more reliable, martensite grains with similar initial line dislocation density (~1×10^{14} m^{-2}) in 9CrODS and T91 were chosen, and the TEM images were taken under similar kinematic diffraction conditions with $\mathbf{g}_{110}$ strongly excited. Fig. 1 shows the in situ TEM observations of the microstructure evolution of 9CrODS versus F/M steel T91. The results of T91 were previously described in detail by Liu et al. [15]. As can be seen from Fig. 1(a)–(e), the dislocation structure in 9CrODS is very stable even after being irradiated to 4.2×10^{15} ions/cm^2 (~7 dpa), as manifested by very low-density black-dot damage accumulation. Similar black-dot dislocation loops have also been reported in previous studies [18,19]. Both the dislocation loops and the Y-Ti-O nanoparticles can appear as dark spots in the bright-field images, but the dislocation loops are distinguishable from the nanoparticles as they appear as bright spots in the corresponding weak-beam dark-field images. One example of this imaging effect can be found in the Supplementary Material. In Fig. 1, several possible black-dot loops were marked by red arrows. The loops remained small black-dots (2–4 nm) and no loop growth was observed up to 7 dpa. Some changes did occur to the pre-existing dislocations, due to dislocation-defect interactions. In addition to the negligible amount of dislocation loops, post-irradiation examination (PIE) also did not find any resolvable voids.

In contrast, as shown in Fig. 1(f)–(j), T91 maintained relative stability only up to around 6.0×10^{14} ions/cm^2 (~1 dpa), and black-dot dislocation loops started to accumulate around 1.8×10^{15} ions/cm^2 (~3 dpa). The black-dot dislocation loops increased in size with increasing dose. One example of loop growth is the loop marked by red circle in Fig. 1 (i) and (j). Loops of 10–20 nm were commonly found after the sample was irradiated to 4.2×10^{15} ions/cm^2. In addition to the buildup of black-dot loops and loop growth, apparent dislocation segments also occurred around 3.0×10^{15} ions/cm^2 (~5 dpa). It is known that in F/M steels, the dislocation segments will evolve into network dislocations, which contribute to irradiation hardening by impeding dislocation motion as well as void swelling by preferentially absorbing interstitials (sink bias) in the high dose regime.

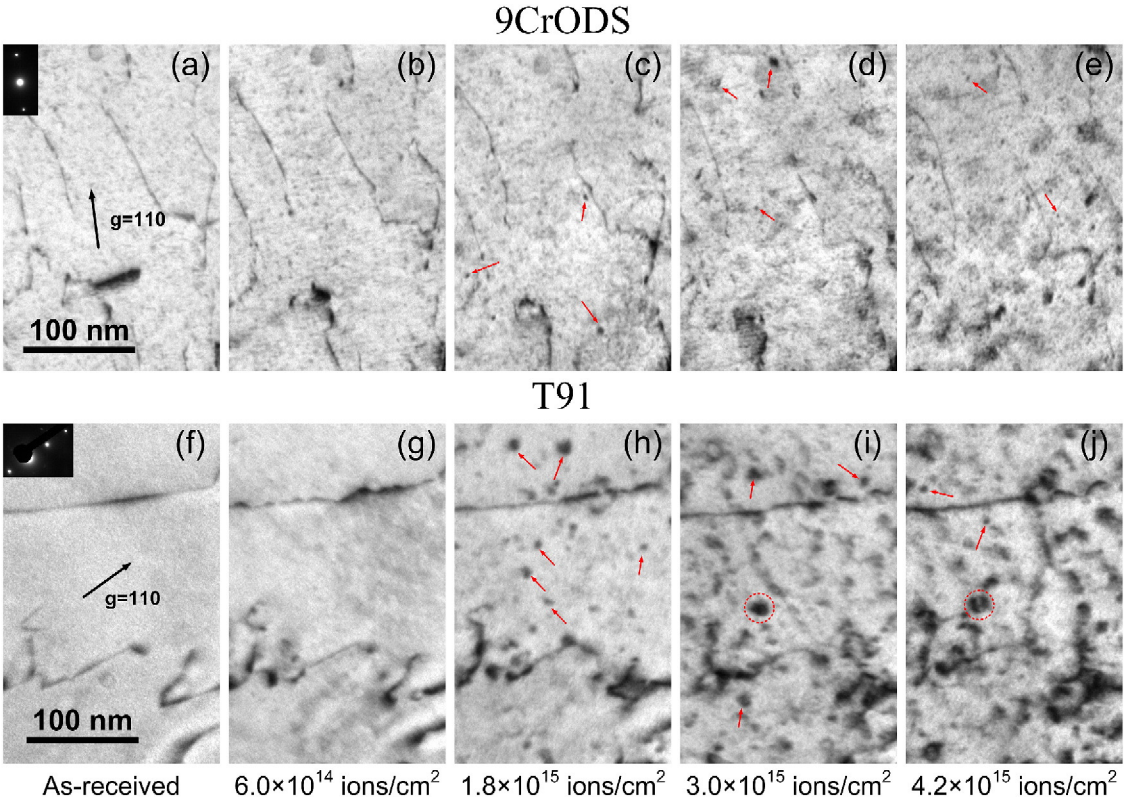

Fig. 1. In situ TEM observations of the microstructure evolution of (a)–(e) 9CrODS, and (f)–(j) F/M steel T91 at various dose levels. Both specimens were irradiated by 1.0 MeV Kr^{++} ions at 400 °C. The T91 result is from previous work [15].

In order to understand the noticeable difference in dislocation structure evolution of 9CrODS versus T91, rate theory calculations were performed using the chemical rate equation [20]:

$$\frac{\partial C_j}{\partial t} = \epsilon_{FM} K_0 - K_{iv} C_i C_v - K_{js} C_j C_s, \quad (1)$$

where $j = i$ or v, ϵ_{FM} is the production efficiency of freely migrating defects (fmd), K_0 is the dpa rate, K is the rate constant for the reaction indicated by the subscripts, C_i, C_v, and C_s are the concentrations of interstitials, vacancies, and sinks, respectively. For F/M steels such as T91, the sinks are pre-existing dislocations and grain boundaries, and Eq. (1) can be written as [20–22]:

$$\frac{\partial C_j}{\partial t} = \epsilon_{FM} K_0 - \frac{4\pi r_{iv}}{\Omega}(D_i + D_v) C_i C_v - \frac{2\pi D_j}{\ln(\mathcal{R}/R_{jd})} C_j \rho_d - \frac{3\pi^2}{L^2} D_j C_j, \quad (2)$$

where ρ_d is the dislocation density, r_{iv} is the defect recombination radius, L is the grain size, $\mathcal{R}$ is defined by $\pi\mathcal{R}^2\rho_d = 1$, R_{jd} is the capture radius for defect j, and D_j is the diffusion coefficient. For ODS alloy, an additional term accounting for the high-density nanoparticles needs to be included:

$$\frac{\partial C_j}{\partial t} = \epsilon_{FM} K_0 - \frac{4\pi r_{iv}}{\Omega}(D_i + D_v) C_i C_v - \frac{2\pi D_j}{\ln(\mathcal{R}/R_{jd})} C_j \rho_d - \frac{3\pi^2}{L^2} D_j C_j - 4\pi r_p D_j C_j \rho_p, \quad (3)$$

where r_p is the nanoparticle-defect capture radius, ρ_p is the number density of the nanoparticles.

For radiation-enhanced diffusion (RED), only considering the contributions from point defects [21]:

$$D_{rad} = f_v D_v C_v + f_i D_i C_i, \quad (4)$$

where f_j is the jump correlation coefficient of defect j ($j = i$ or v).

Table 2 lists the input parameters for rate theory calculations. The parameters are from recent work on modeling radiation-induced segregation (RIS) in F/M alloys [23] and previous rate theory studies [20–22,24,25].

Fig. 2 shows the calculated radiation enhanced diffusivity D_{rad} for four cases: (1) recombination only ($C_s \approx 0$), (2) sink 1: recombination with dislocation and grain boundary sinks only, (3) sink 2: recombination with nanoparticle sinks only, and (4) sink 3: recombination with dislocation, GB, and nanoparticle sinks. The chosen parameters such as dislocation density, grain size, nanoparticle size and number density are consistent with commonly reported values in F/M steels and ODS steels. As reference, the thermally-activated diffusivity D_{th} is also plotted in Fig. 2.

Table 2
Input parameters for rate theory calculations.

Parameter	Value
fmd production efficiency, ϵ_{FM}	0.04 [21]
Vacancy jump correlation factor, f_v	0.727 [21,23]
Interstitial jump correlation factor, f_i	0.727 [21,23]
Vacancy Debye frequency, ν_v	1.5×10^{13} s^{-1} [23]
Interstitial Debye frequency, ν_i	1.5×10^{12} s^{-1} [23]
Vacancy formation energy of Cr, E_{fv}^{Cr}	2.25 eV [23]
Vacancy migration energy of Cr, E_{mv}^{Cr}	0.55 eV [23]
Vacancy formation energy of Fe, E_{fv}^{Fe}	1.6 eV [23]
Vacancy migration energy of Fe, E_{mv}^{Fe}	0.63 eV [23]
Interstitial migration energy of Cr, E_{mi}^{Cr}	0.28 eV [23]
Interstitial migration energy of Fe, E_{mi}^{Fe}	0.35 eV [23]
Lattice constant, a	0.288 nm [26]
Burgers vector, b	0.249 nm [26]
Atomic volume, Ω	0.012 nm^3 [25]
Recombination volume, $\frac{4}{3}\pi r_{iv}^3$	100 Ω [20]
Dislocation density, ρ_d	10^{14} m^{-2} [15]
Dislocation-vacancy capture radius, R_{vd}	4b [24]
Dislocation-interstitial capture radius, R_{id}	10b [24]
Nanoparticle number density, ρ_p	10^{23} m^{-3}
Nanoparticle defect capture radius, r_p	2.0 nm

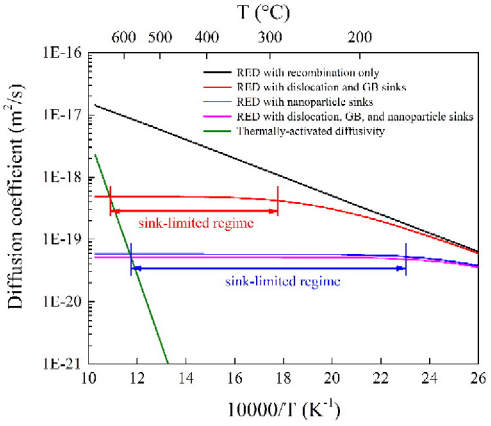

Fig. 2. Calculated diffusion coefficient for thermally-activated diffusion and radiation-enhanced diffusion with various sinks.

As can be seen from Fig. 2, the D_{rad} for recombination only follows Arrhenius behavior with an activation energy of half of the vacancy migration energy E_{mv}. The D_{rad} in black well represents most solution annealed Fe-Cr model alloys that have coarse grains and low dislocation densities (~10^{11} m^{-2}). The introduction of dislocations and GBs into the material effectively reduces the D_{rad} and the sink-limited regime lies in the ~290 °C to 630 °C range, as shown in the red curve. This represents the case for most ferritic/martensitic steels that have high dislocation density and small grain size. In comparison, the nanoparticle sinks are much more efficient in suppressing D_{rad}, as the D_{rad} in blue is about one order of magnitude lower than the D_{rad} in red at temperatures where RED dominates. The temperature range of the sink-limited regime is also lowered to ~150 °C to 560 °C. For ODS steels, the nanoparticles play the dominant role in suppressing RED, as further including the dislocations and GBs sinks only helps slightly in suppressing RED (the D_{rad} in pink is only slightly lower than the D_{rad} in blue).

Further comparison can be made for the concentration of freely migrating defects (fmd). The dislocation-vacancy and dislocation-interstitial capture radii in Table 2 are different, which is known as the sink bias. Fig. 3 shows the calculated relative defect concentration (absolute concentration divided by the concentration of the recombination only case). The vacancy/interstitial concentrations are named by their subscripts: v represents vacancy and i represents interstitial, r is the recombination only ($C_s \approx 0$) case, aforementioned sink 1, 2, 3 cases are denoted by s1, s2, s3, respectively.

As can be seen from Fig. 3, the fmd concentrations of s2 and s3 cases are significantly lower than the s1 case. Table 3 lists the vacancy and interstitial concentrations (in atomic fraction) for different sinks at 400 °C, the irradiation temperature for T91 and 9CrODS. For sink 1, C_{is1}/C_{ir} is 0.145, whereas C_{vs1}/C_{vr} is about 0.176. The 21% difference is due to the sink bias of dislocations ($B \approx 0.29$). For sink 2, both C_{is2}/C_{ir} and C_{vs2}/C_{vr} are about 0.019. For sink 3, C_{is3}/C_{ir} is 0.0168 and C_{vs3}/C_{vr} is 0.0176. F/M steel T91 and 9CrODS steel can regarded approximately belongs to sink 1 and sink 3 case, respectively. Therefore, the fmd defect concentration of the 9CrODS alloy is about one order of magnitude smaller than that of the T91 alloy, due to the existance of nanoparticle sinks. Indicating that the high-density nanoparticles in ODS steels are much more efficient in absorbing point defects and suppressing the buildup of defect clusters. In contrast, the dislocations and GBs at the calculated density level play less important role in terms of point defect annihilation.

The aforementioned results assume a constant dislocation density and did not take into account the buildup of defect clusters at different dose levels. The exact solution of the surviving fmds and RED requires

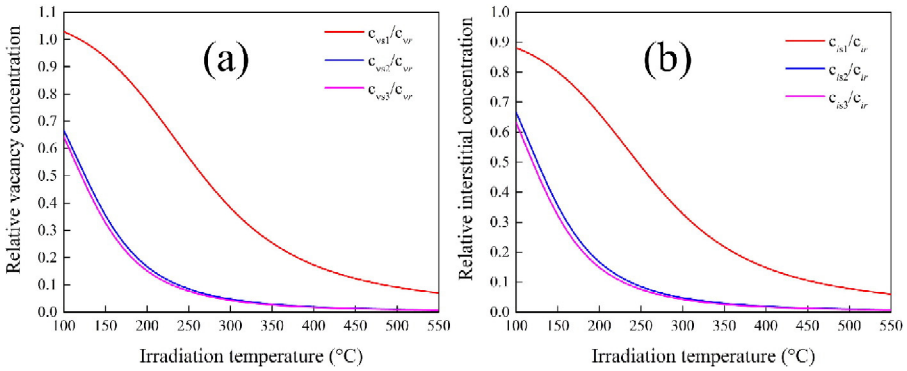

Fig. 3. Calculated relative (a) vacancy concentration and (b) interstitial concentration for sink 1: dislocations and GBs, sink 2: nanoparticles, and sink 3: nanoparticles, dislocations, and GBs. The concentrations are normalized by the recombination-only ($C_s \approx 0$) defect concentrations.

coupled defect balance equations that can model the evolution of defect clusters. However, the coupling of dose-dependent defect clusters and dislocation densities should not change our order-of-magnitude analysis. As a simple estimation of the influence of dislocation density on the radiation-enhanced diffusion coefficient for sink 1, calculations were made at three different dislocation densities and the results can be found in the Supplementary Material. For T91 irradiated at 400 °C up to 7 dpa, the defect concentrations may be smaller by a factor of 2 than the ones for sink 1 in Table 3.

In summary, the superior radiation stability of a 9CrODS steel is demonstrated through the direct comparison with a 9Cr F/M steel T91 using in situ TEM heavy ion irradiation. For the irradiation at 400 °C up to 7 dpa, 9CrODS maintained overall microstructure stability with much less black-dot dislocation loops, in contrast to various changes such as rapid buildup of dislocation loops, loop growth, and formation of dislocation segments observed in non ODS alloy T91. Rate theory calculations found that compared to dislocations (~10^{14} m^{-2}) and GBs, the high-density (~10^{23} m^{-3}) nanoparticles in ODS steels are much more efficient in removing point defects and suppressing the buildup of defect clusters. The RED of the 9CrODS steel enters the sink-limited regime above ~150 °C, and is also greatly suppressed compared to that of the non-ODS F/M steel T91.

Acknowledgements

The authors would like to thank IVEM staff Pete Baldo and Edward Ryan at Argonne National Laboratory for their assistance with the irradiation experiments. Xiang Liu would also like to thank Professor Pascal Bellon at the University of Illinois at Urbana-Champaign for his instructions on rate theory calculations. This work was funded by the DOE Office of Nuclear Energy's Nuclear Energy University Program (NEUP) under Contract No. DE-NE0008291. The in situ ion irradiation was accomplished at Argonne National Laboratory at the IVEM-Tandem Facility, a U.S. Department of Energy Facility funded by the DOE Office of Nuclear Energy, operated under Contract No. DE-AC02-06CH11357 by UChicago Argonne, LLC and the DOE Office of Nuclear Energy under DOE Idaho Operations Office Contract DE-AC07-051D14517 as part of a Nuclear Science User Facilities experiment.

Table 3
Calculated vacancy and interstitial concentrations (in atomic fraction) for different sinks at 400 °C.

	C_i	C_v
$C_s \approx 0$	2.2E−9	6.8E−8
Sink 1	3.2E−10	1.2E−8
Sink 2	4.2E−11	1.3E−9
Sink 3	3.7E−11	1.2E−9

Appendix A. Supplementary data

Supplementary data to this article can be found online at https://doi.org/10.1016/j.scriptamat.2018.01.018.

References

[1] G.R. Odette, M.J. Alinger, B.D. Wirth, Annu. Rev. Mater. Res. 38 (2008) 471–503.
[2] G. Zhang, Z. Zhou, K. Mo, P. Wang, Y. Miao, S. Li, M. Wang, X. Liu, M. Gong, J. Almer, J. F. Stubbins, J. Alloys Compd. 648 (2015) 223–228.
[3] K.A. Unocic, B.A. Pint, D.T. Hoelzer, J. Mater. Sci. 51 (2016) 9190–9206.
[4] Y. Miao, K. Mo, Z. Zhou, X. Liu, K.-C. Lan, G. Zhang, M.K. Miller, K.A. Powers, J.F. Stubbins, J. Nucl. Mater. 480 (2016) 195–201.
[5] M.K. Miller, D.T. Hoelzer, E.A. Kenik, K.F. Russell, Intermetallics 13 (2005) 387–392.
[6] E. Aydogan, N. Almirall, G.R. Odette, S.A. Maloy, O. Anderoglu, L. Shao, J.G. Gigax, L. Price, D. Chen, T. Chen, F.A. Garner, Y. Wu, P. Wells, J.J. Lewandowski, D.T. Hoelzer, J. Nucl. Mater. 486 (2017) 86–95.
[7] N.A. Bailey, E. Stergar, M. Toloczko, P. Hosemann, J. Nucl. Mater. 459 (2015) 225–234.
[8] A. Certain, S. Kuchibhatla, V. Shutthanandan, D.T. Hoelzer, T.R. Allen, J. Nucl. Mater. 434 (2013) 311–321.
[9] T. Chen, J.G. Gigax, L. Price, D. Chen, S. Ukai, E. Aydogan, S.A. Maloy, F.A. Garner, L. Shao, Acta Mater. 116 (2016) 29–42.
[10] M.K. Miller, D.T. Hoelzer, J. Nucl. Mater. 418 (2011) 307–310.
[11] J. Ribis, S. Lozano-Perez, J. Nucl. Mater. 444 (2014) 314–322.
[12] X. Liu, Y. Miao, Y. Wu, S.A. Maloy, J.F. Stubbins, Scr. Mater. 138 (2017) 57–61.
[13] L.L. Hsiung, M.J. Fluss, S.J. Tumey, B.W. Choi, Y. Serruys, F. Willaime, A. Kimura, Phys. Rev. B Condens. Matter Mater. Phys. 82 (2010) 1–13.
[14] O. Anderoglu, T.S. Byun, M. Toloczko, S.A. Maloy, Metall. Mater. Trans. A 44 (2013) 70–83.
[15] X. Liu, Y. Miao, M. Li, M.K. Kirk, S.A. Maloy, J.F. Stubbins, J. Nucl. Mater. 490 (2017) 305–316.
[16] J.F. Ziegler, M.D. Ziegler, J.P. Biersack, Nucl. Instrum. Methods Phys. Res. Sect. B Beam Interact. Mater. Atoms 268 (2010) 1818–1823.
[17] R.E. Stoller, M.B. Toloczko, G.S. Was, A.G. Certain, S. Dwaraknath, F.A. Garner, Nucl. Instrum. Methods Phys. Res. Sect. B Beam Interact. Mater. Atoms 310 (2013) 75–80.
[18] G. Gupta, Z. Jiao, A.N. Ham, J.T. Busby, G.S. Was, J. Nucl. Mater. 351 (2006) 162–173.
[19] A. Ramar, N. Baluc, R. Schäublin, J. Nucl. Mater. 367–370 (2007) 217–221.
[20] R. Sizmann, J. Nucl. Mater. 69–70 (1978) 386–412.
[21] G.S. WAS, Fundamentals of Radiation Materials Science, Springer New York, New York, NY, 2017.
[22] K. Tai, R.S. Averback, P. Bellon, Y. Ashkenazy, B. Stumphy, J. Nucl. Mater. 422 (2012) 8–13.
[23] J.P. Wharry, G.S. Was, Acta Mater. 65 (2014) 42–55.
[24] E. Kuramoto, T. Tsutsumi, J. Nucl. Mater. 212–215 (1994) 175–178.
[25] Z.N. Ding, C.H. Zhang, Y.T. Yang, Y. Song, A. Kimura, J. Jang, J. Nucl. Mater. 493 (2017) 53–61.
[26] W.-Y. Chen, Irradiation Damage in Neutron-Irradiated FeCr Model Alloys, University of Illinois at Urbana-Champaign, 2014.